



Interaction of microseisms with crustal heterogeneity: A case study from the San Jacinto fault zone area

G. Hillers

*Institut des Sciences de la Terre, Université Joseph Fourier, CNRS,
Grenoble, France (gregor.hillers@ujf-grenoble.fr)*

Y. Ben-Zion

Department of Earth Sciences, University of Southern CA, Los Angeles, USA

M. Landès

Institut de Physique du Globe de Paris, Paris, France

M. Campillo

*Institut des Sciences de la Terre, Université Joseph Fourier, CNRS,
Grenoble, France*

[1] We perform a multicomponent analysis to evaluate the validity and limits of noise imaging in the San Jacinto fault zone (SJFZ) area. Estimates of noise propagation and scattering length scales in the area are combined with a noise correlation-based analysis of variability of noise constituents, excitation regions, and propagation patterns. We evaluate the quality of correlation-phase and -amplitude imaging of tectonic features in the context of observed noise properties. Statistical properties of a regional high-resolution 3-D velocity model indicate that propagation of double-frequency microseism Rayleigh waves is sensitive to medium heterogeneity in the southern California plate boundary area. The analysis of noise correlation functions constructed from records of a regional seismic network suggests stable excitation of microseisms along the southern California coastline. The proximity to the source region together with randomization properties of the heterogeneous medium govern the scattered yet anisotropic character of the wave field. Insignificant travel time errors resulting from the associated imperfect reconstruction of interstation Green's function estimates allow the resolution of a velocity contrast across the SJFZ from noise correlations. However, attenuation estimates are biased by the anisotropic propagation directions. The interaction of the ambient surface wave field with medium heterogeneity facilitates imaging of the velocity structure, but the inversion of the amplitude pattern is limited since it is dominated by wave field instead of medium properties.

Components: 11,107 words, 10 figures, 1 table.

Keywords: noise correlations; microseism wave field; noise-based imaging; crustal scattering; mean free path.

Index Terms: 7205 Seismology: Continental crust; 3285 Mathematical Geophysics: Wave propagation; 8015 Structural Geology: Local crustal structure.

Received 5 October 2012; **Revised** 21 March 2013; **Accepted** 5 April 2013; **Published** 19 July 2013.

Hillers, G., Y. Ben-Zion, M. Landès, and M. Campillo (2013), Interaction of microseisms with crustal heterogeneity: A case study from the San Jacinto fault zone area, *Geochem. Geophys. Geosyst.*, 14, 2182–2197, doi:10.1002/ggge.20140.

1. Introduction

[2] Fault zone environments have complex 3-D distributions of seismic velocities and attenuation coefficients, with hierarchical damage zones and at places prominent bimaterial interfaces [e.g., *Ben-Zion and Sammis, 2003*]. The damage structures includes zones of several kilometers or more of reduced elastic moduli and velocities [e.g., *Fialko et al., 2002; Allam and Ben-Zion, 2012*], regions of elevated scattering [e.g., *Revenaugh, 2000; Carcolé and Sato, 2010; Zheglova et al., 2012*], and intense internal damage producing trapped waves and related signals [e.g., *Ben-Zion and Aki, 1990; Li et al., 1994; Lewis and Ben-Zion, 2010; Yang and Zhu, 2010*]. Fault bimaterial interfaces are seen clearly with head waves that refract along the interface [e.g., *Ben-Zion and Aki, 1990; McGuire and Ben-Zion, 2005; Bulut et al., 2012*], and velocity contrasts in images based on earthquake tomography [e.g., *Eberhart-Phillips and Michael, 1993; Thurber et al., 2006*] and teleseismic data [*Ozakin et al., 2012*].

[3] Ambient seismic noise provides additional useful signals for imaging fault zone structures [e.g., *Roux et al., 2005; Hong and Menke, 2006*]. Noise-based techniques are especially useful in regions of no or low seismicity, and allow imaging of velocity structures with a resolution only limited by the network geometry and frequency-dependent properties of the ambient wave field [e.g., *Shapiro and Campillo, 2004*]. In regions with relatively high background seismicity, ambient noise can complement results from earthquake studies by providing a potentially more homogeneous spatial resolution; surface wave studies allow detailed imaging of shallow structures essential for improved assessment of near-fault strong ground shaking.

[4] Focusing on double-frequency (DF; $\sim 5\text{--}7$ s) microseisms we perform a joint analysis of scattering length scales and noise anatomy to evaluate the validity and limits of various components of noise imaging in the San Jacinto fault zone (SJFZ) environment (Figure 1). In section 2, we analyze the relevant propagation and scattering length scales associated with DF Rayleigh waves. Heterogeneity and scattering estimates are derived from a regional high-resolution 3-D velocity model; this component constitutes a key observation for noise-based imaging in the southern California plate boundary area. In section 3, we analyze noise correlation (C -) functions associated with a regional network to study the seasonal variability of domi-

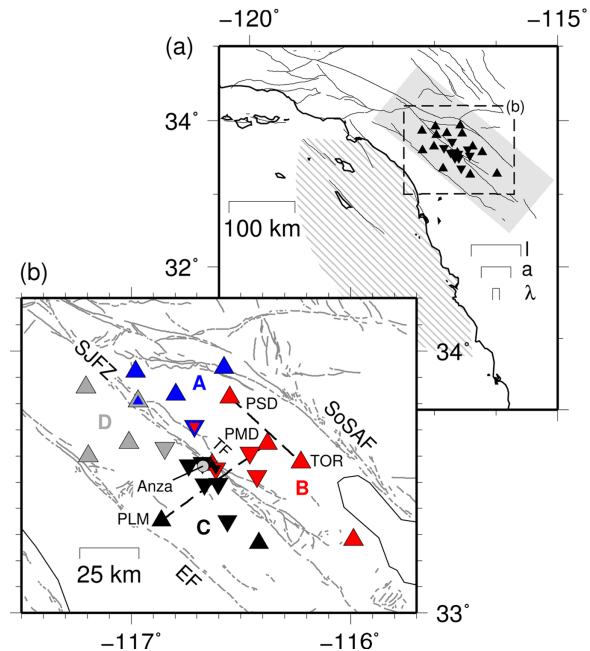


Figure 1. Overview of the study area. (a) This map shows the propagation and scattering length scales (equation (3)). The hatched area shows the estimated source region. The gray rectangle shows the dimension of the velocity model from which $P(k)$ (equation (2)) is estimated. (b) The map shows CISN (triangles) and Anza network (inverted triangles) stations. The dashed lines connect the station pairs in Figure 5. Colors indicate subarrays A–D used in section 4. SJFZ: San Jacinto fault zone. EF: Elsinore fault. SoSAF: Southern San Andreas fault. TF: Trifucation area.

nant wave field constituents, excitation regions, and propagation patterns. The main part of the analysis is then completed by discussing the C -function based results in the context of estimated propagation and scattering properties. In section 4, we discuss the implications of the joint length-scale and wave field analysis on noise imaging in the SJFZ area. Phase and amplitude information from C -functions are used to test the validity of noise-based velocity and attenuation estimates, respectively.

2. Scattering Length Scales

[5] Scattering properties of the medium control the characteristics of the ambient wave field at long lapse times [e.g., *Paul et al., 2005; Campillo, 2006; Larose et al., 2008*] and are usually estimated from earthquake coda properties [e.g., *Sato et al., 2012*, and references therein]. In contrast to coda analyses, we can draw upon a recently resolved tomographic image of medium heterogeneity in the southern California plate boundary

area [Allam and Ben-Zion, 2012] to derive DF Rayleigh wave scattering properties in a volume around the SJFZ. We estimate the correlation length of medium fluctuations a , scattering attenuation Q_{sc} , and the associated elastic or scattering mean free path l from the spatial distribution of velocity variations $\delta c/c = (\delta c/c)_\omega$. Estimates of a indicate the sensitivity of a given wave number to the spatial heterogeneity; l is a typical length scale for the average distance between two scattering events of a wave front propagating through the heterogeneous medium [Aki and Richards, 1980; Campillo, 2006]. In other words, l is the unit distance for a fractional energy loss through scattering for a seismic wave at wave number k and is related to Q_{sc} by

$$l = \frac{Q_{sc}(k)}{k}. \quad (1)$$

[6] In the far field of a (single) scattering region with weak velocity perturbations Q_{sc}^{-1} can be estimated using [Frankel and Clayton, 1986; Wegler, 2003]

$$Q_{sc}^{-1}(k) = 2k^2 \sigma^2 \int_{\theta_{\min}}^{\pi} P(k_r) d\theta. \quad (2)$$

[7] The scaled spectral power density $P(k)$ of the radial wave number k_r characterizes the fluctuation statistics of spatial random fields in the Fourier domain, σ^2 denotes the variance of the 2-D velocity fluctuation distribution, and θ indicates the azimuthal forward scattering angle. We estimate $P(k)$ associated with Rayleigh wave $\delta c/c$ data (Figure 2a) inferred from v_P, v_S tomography results [Allam and Ben-Zion, 2012, see Appendix for processing details]. $P(k)$ and hence Q_{sc} and l estimates correspond to a radial average of me-

dium heterogeneity. The spectra $P(k)$ constitutes an average across prominent anisotropic $\delta c/c$ features like the Salton trough, the high- and low-velocity zones across the fault, or the elongated low-velocity zone associated with the SJFZ. The scattering potential is probably sensitive to the propagation direction, which is, however, not further investigated here.

[8] Fluctuation statistics of random media are usually parameterized by models in which the associated spectra are flat from zero to 2π times the inverse of the isotropic correlation length a ; i.e., for $ka < 1$ the medium appears homogeneous, whereas spectral decay properties at $ka > 1$ control the high-wave number characteristics of a distribution relevant for scattering. We fit von Karman, exponential, and Gaussian models to $P(k)$ functions associated with $\delta c/c$ distributions [Frankel and Clayton, 1986; Holliger and Levander, 1992; Mai and Beroza, 2002]. Fitting parameters for all models include the correlation distance $k_c = 2\pi/a$, the spectral low-frequency level A_0 for $k < k_c$, and the Hurst exponent H for the von Karman model. We note that A_0 depends on σ^2 , which is not explicitly given in the 2-D Fourier Transform expressions in e.g., Frankel and Clayton [1986]; A_0 is thus associated with the mean square of the fractional velocity fluctuation, elsewhere denoted ε^2 [e.g., Nishizawa and Fukushima, 2008]. Linear least-squares fits reveal the superior performance of the von Karman model compared to other parameterizations [Holliger and Levander, 1992; Sato and Fehler, 2008]. For 5 s (2 s) Rayleigh waves (Figure 2b) we infer $a = 44$ km ($a = 38$ km) and $H = 1.2$ (1.2), which is comparable to $a = 25$ km inferred for 1 Hz teleseismic P waves in southern California [Powell and Meltzer, 1984]. The best-fitting exponential model shows a larger discrepancy with $P(k)$, while the Gaussian model is not compatible with the data considering an order-of-magnitude larger error.

[9] Referring to the von Karman parameterization, the correlation length is larger than the DF Rayleigh wave length λ , i.e., $a > \lambda$ or $ka > 1$. We iterate that the dense network and high-seismicity rates in the study area facilitate the construction of an image of medium heterogeneity [Allam and Ben-Zion, 2012]. This makes the scattering length-scale analysis possible, from which we conclude that propagation of DF microseism Rayleigh waves is sensitive to the scale of crustal heterogeneity. Moreover, the relative high resolution of the image (1 km^3) allows the integration over the decaying $P(k)$ amplitudes for the relevant wave numbers to estimate l .

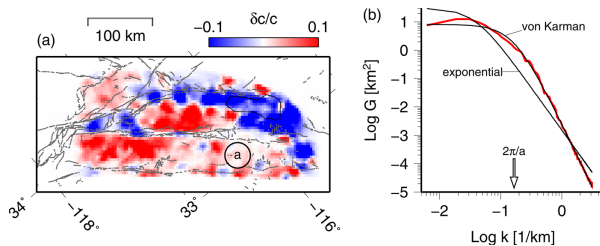


Figure 2. (a) Spatial $\delta c/c$ fluctuations in the study area for a 2 s Rayleigh wave are derived from the velocity model of Allam and Ben-Zion [2012] and equation (A6). The circle indicates the associated von Karman correlation length a . (b) The corresponding distribution of the unscaled power spectral density $G(k)$ (red; $P(k) = G(k)/\sigma^2$, see Appendix) is best fitted with a von Karman model.

[10] These estimates are controlled by the choice of θ_{\min} (equation (2)). An appropriate value of θ_{\min} is unclear and has been a matter of dispute [Sato and Korn, 2008]. Some constraint on θ_{\min} , i.e., $\theta_{\min} \approx 30^\circ$, comes from comparisons of synthetic amplitude decay rates to theoretical predictions based on equation (2) [Frankel and Clayton, 1986]. Results in Table 1 show that for small lower cutoff angles ($\theta_{\min} \leq 20^\circ$) l is proportional to period; for larger angles, the pattern does not show a frequency dependence; higher frequencies have a greater sensitivity to choices of θ_{\min} (Q_{sc} estimates are discussed in section 5). Focusing on the $T=5$ s results for $\theta_{\min} \geq 20^\circ$ we find that estimates of the scattering mean free path are larger than the correlation distance, $l > a$. Recall that this result is not only controlled by the shape of the $P(k)$ high-frequency falloff, but also by σ^2 , the variance of the medium fluctuations.

[11] To conclude our analysis of relevant propagation and scattering length scales we anticipate results from section 3, where we show that the DF surface wave source region is associated with near coastal waters off southern California. We find that the average distance d of the study area, or the network, to the noise excitation region is compatible with or only slightly larger than the scattering mean free path, $d \geq l$ (Figure 1a). Our analysis can be summarized by the relation

$$d \geq l > a > \lambda. \quad (3)$$

[12] While all three individual length-scale relations are important in the present context, $d \geq l$ has perhaps the strongest implication for the properties of the ambient seismic wave field in the study area: We can expect that the randomization of microseism propagation directions is relatively weak, characterized by mostly a few scattering events between excitation and observation. Wave field equipartition, theoretically required to reconstruct Green's function estimates utilized in noise imaging [e.g., Campillo, 2006], is therefore unlikely to be observed; yet

heterogeneity furthers mixing and promotes scattered over ballistic propagation. We thus anticipate the limits of noise imaging in the SJFZ area to be associated with the proximity to the noise excitation region.

3. Wave Field Properties from Noise Correlations

[13] The propagation and scattering length scales summarized by equation (3) determine the framework for each imaging study in the SJFZ area based on processing of microseisms. To extend our investigation of factors controlling the quality of potential reconstructed images we proceed with an analysis of noise recordings. In this section, we study the seasonal variability of dominant wave field constituents, noise source regions, and propagation and excitation patterns using noise correlation functions.

3.1. Data Processing

[14] We use data from 24 stations of the California Integrated Seismic Network and the Anza network in the SJFZ area (Figure 1b). Continuous 40 Hz broadband three-component data are retrieved for two 100 day northern hemispheric winter and summer periods, respectively. Winter periods start 1 December 2008 and 2009. Summer periods begin 1 June 2009 and 2010. We analyze properties of correlation functions in three frequency (f) bands: 0.1–0.45, 0.1–1.3, and 0.7–1.3 Hz; the low-frequency band contains DF microseisms, whereas higher frequencies were used to target a crustal P wave [Roux *et al.*, 2005]. We limit our analysis of wave field properties to the DF band due to the superior signal strength.

[15] After instrument response removal time series are whitened and amplitudes are clipped at three times the standard deviation of daily amplitude distributions. Daily correlation functions, consisting of 24 hourly stacks [Seats *et al.*, 2012; Hillers *et al.*, 2012a], from the two respective winter and summer periods are stacked to obtain averaged vertical-vertical (ZZ) and vertical-radial (ZR) winter, summer, and all-season (winter and summer) correlations (Figure 3). The radial component is determined by rotating the North and East components into the great circle connection between two stations, in contrast to Roux [2009] and Roux *et al.* [2011] who used an Optimal Rotation Algorithm to mitigate effects associated with strongly anisotropic energy flux.

Table 1. Dependence of Scattering Attenuation Q_{sc} and the Scattering Mean Free Path l on θ_{\min} (equation (2)) and Period T

T	θ_{\min}			
	15°	20°	25°	30°
2 s	23/19	58/48	124/103	201/166
5 s	15/33	22/50	32/71	46/102
10 s	18/92	23/120	30/151	37/188

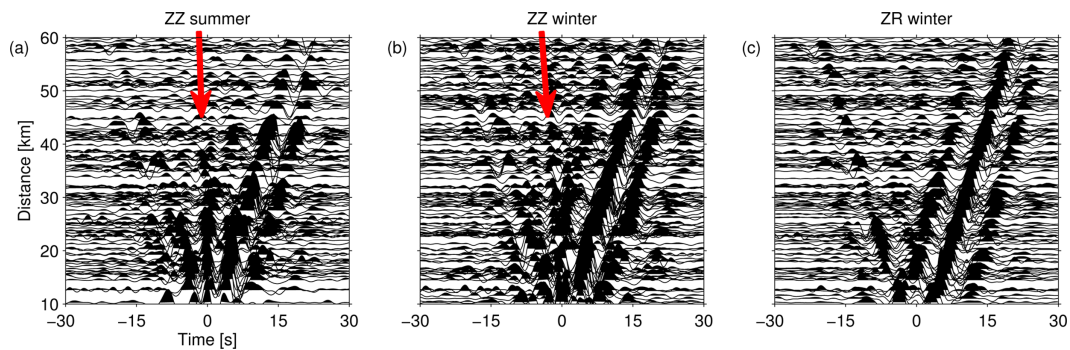


Figure 3. Time-distance plots of correlations exhibit one or two arrivals. (a) ZZ summer stacks are dominated by the Rayleigh wave, but also contain a teleseismic body wave characterized by large apparent velocity and small amplitude (arrow). (b) ZZ winter stacks contain the Rayleigh wave, and the teleseismic body wave with larger amplitude yet smaller apparent velocity compared to Figure 3a. (c) ZR winter stacks contain only Rayleigh wave energy. Correlations associated with coast- and fault-perpendicular station bearings are organized such that waves traveling away from the coast appear at positive lags. (For illustrative purposes, the number of traces is limited to 10 per 5 km interval, at the expense of low amplitude, yet more symmetric, coast-parallel correlations.)

3.2. Wave Field Constituents

3.2.1. Rayleigh Wave

[16] Distance dependent 5 s ZZ and ZR arrival patterns are dominated by a Rayleigh wave traveling at average 2.8 km/s (Figure 3). DF Rayleigh waves are generated by opposite traveling components of the ocean surface wave field [Longuet-Higgins, 1950, 1953]. Such conditions can be associated with the wave field of storm systems [Kedar *et al.*, 2008; Zhang *et al.*, 2010; Kedar, 2011], with reflections off floating icebergs [Ardhuin *et al.*, 2011], and with near coastal interactions between incoming and reflected wave fields [e.g., Haubrich and McCamy, 1969; Friedrich *et al.*, 1998; Bromirski and Duennebieer, 2002; Essen *et al.*, 2003]. Application of a correlation-based beam-forming approach [Landès *et al.*, 2010] to northern hemispheric winter and summer ZZ correlations reveals the seasonally stable excitation of DF microseisms off the southern California coast (Figure 4) [Schulte-Pelkum *et al.*, 2004; Stehly *et al.*, 2006; Tanimoto *et al.*, 2006]. Correlation amplitudes are larger during winter months, reflecting an increased coherency associated with stronger atmospheric disturbances and hence excitation. The proximity of the observation area to the noise source region together with insufficient randomization through scattering inferred in section 2 leads to an asymmetric surface wave amplitude pattern for coast perpendicular station bearings (Figures 3 and 5a) [Sabra *et al.*, 2005a]. Simultaneously, Rayleigh wave amplitudes at coast-parallel bearings are reduced relative to amplitudes associated with a near-zero arrival (Figure 5c) discussed next.

3.2.2. Teleseismic Body Wave

[17] In addition to the laterally propagating surface wave, a near vertically incident arrival of high-apparent velocity emerges in ZZ but not in ZR correlations (Figures 3c and 5c). The associated slowness pattern shows a seasonal dependence. A proper understanding of this arrival is important to characterize the ambient wave field constituents for the assessment of potentially biased Rayleigh arrival times in *C*-functions of closely spaced stations.

[18] Longitudinally polarized particle motions (Figure 5d) indicate teleseismic body waves. This interpretation is further supported by maps of the signal amplitude in the horizontal slowness domain (Figure 4). The hypothesis of ballistic arrivals discussed by Roux [2009], van Wijk *et al.*

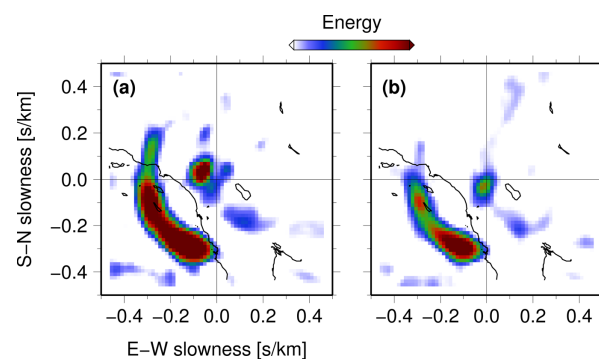


Figure 4. Results of the correlation-based beam-forming analysis, (a) ZZ winter and (b) summer stacks (0.1–0.45 Hz). The center of the slowness maps aligns with the network center.

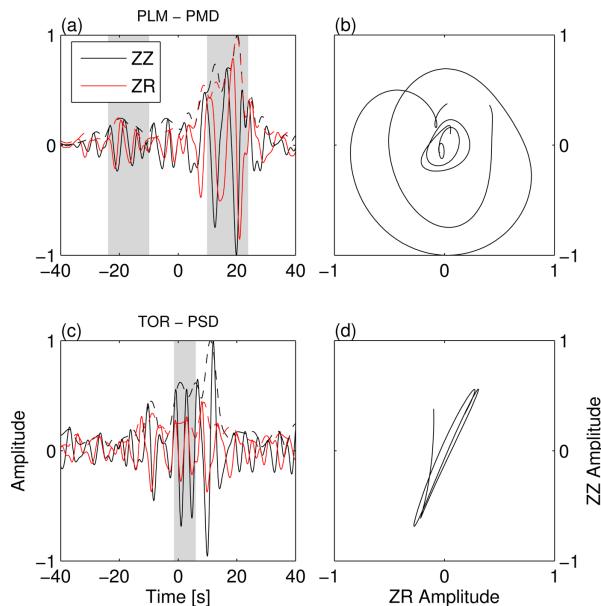


Figure 5. Correlation amplitudes depend on the station orientation relative to the predominant noise propagation direction. Amplitudes are scaled to the maximum envelope (dashed lines) in each figure. See Figure 1b for propagation paths. (a) Flux-parallel C -functions are characterized by an asymmetric arrival pattern. Large amplitudes at positive lags correspond to energy traveling from southwest to northeast. (b) The corresponding particle motions illustrate the circular polarization. (c) Rayleigh wave amplitudes in flux-perpendicular correlations are significantly reduced. (d) The correlation contains a relatively strong teleseismic body wave with longitudinal polarization, indicating an almost vertically incident phase. Correlations are winter stacks in the 0.1–0.45 Hz range. Data in Figures 5band 5d are taken from the gray-indicated time window in Figures 5a and 5c, respectively.

[2011], and Hillers *et al.* [2012a] can thus be rejected in this case. The body wave slowness pattern corresponds to microseism excitation that follows the global weather pattern [e.g., Haubrich and McCamy, 1969; Schulte-Pelkum *et al.*, 2004; Stehly *et al.*, 2006; Landès *et al.*, 2010; Hillers *et al.*, 2012b; Stutzmann *et al.*, 2012]. Application of the backprojection method from Landès *et al.* [2010] indicates that teleseismic arrivals during northern (southern) hemispheric winter months result from excitation in the North Pacific (Southern Ocean), consistent with observations by Landès *et al.* [2010] and predictions by Kedar *et al.* [2008] and Hillers *et al.* [2012b].

[19] The analysis of amplitude patterns does not reveal the existence of a crustal P phase [Roux *et al.*, 2005; Zhang *et al.*, 2009]. Hence surface wave energy is not or only weakly scattered into body wave energy that is coherent across the net-

work [Roux *et al.*, 2005], and the atmosphere-ocean-seafloor interactions discussed by Zhang *et al.* [2009] are less likely to occur off the southern California coast.

3.3. Intensity Distributions

[20] The C -function signal-to-noise ratio (SNR) pattern provides further information on regional wave field properties, complementary to the results obtained with correlation-based beamforming. We show how SNR distributions can be translated into azimuthally variable noise intensity pattern. This information is essential to estimate arrival time errors, δt , and thus key to our correlation-based evaluation of the validity and limits of noise imaging in the SJFZ area.

[21] SNR estimates [Sabra *et al.*, 2005b] are controlled by the constituents of the ambient wave field but are also sensitive to preprocessing choices. Particularly in this seismically active region, SNR levels can potentially benefit from alternative processing strategies or parameter choices for data segments containing earthquake signals. The SNR can be parameterized using [Larose *et al.*, 2007]

$$\text{SNR} = B \sqrt{\frac{\tau c \Delta f}{r^e f_c}}. \quad (4)$$

[22] For each frequency band, the ratio of the product of correlation time τ , wave speed c , and bandwidth Δf to the central frequency f_c is constant. For a given realization constituting station distance r and fit exponent e , the SNR level is controlled by the noise intensity $B(\theta)$ as defined in Weaver *et al.* [2009] and Froment *et al.* [2010]. $B(\theta)$ is a measure of coherent relative to incoherent energy propagating along a station connection that varies azimuthally since isotropy as an asymptotic limit is not realized in an open system like the crust of the Earth. Consequently, a reconstructed Green's function amplitude is related to B along the alignment of the end-fire lobes [Froment *et al.*, 2010], “areas in which the phase of the correlation function of direct waves is stationary with respect to azimuth” [Gouédard *et al.*, 2008].

[23] All quantities in the $\sqrt{\quad}$ -term of equation (4) are known except the decay parameter e . It is found by fitting r^e to $\text{SNR}(r)$ data. The residuals are estimates of $B(r)$, and the $B(\theta)$ distribution is found by choosing the station bearing instead of the distance associated with an individual

measurement. $B(\theta)$ is a local measure and can change with increasing distance from a source region due to—locally isotropic—attenuation; here ‘local’ refers to a network average and does not take possible network internal B variations, e.g., through scattering, into account.

[24] Figure 6 shows smoothed $B(\theta)$ patterns, where smoothing choices are related to the distance- and frequency-dependent size of the end-fire lobes [Roux *et al.*, 2004; Weaver *et al.*, 2009; Froment *et al.*, 2010]. The distributions have maximum values in the southwest quadrant, with a peak around 210° , which is approximately perpendicular to the strike of the coast southwest of the network [Sabra *et al.*, 2005a]. The pattern is consistent with the beam-forming generated slowness maps (Figure 4). Smaller contributions arriving from the southeast are likely associated with excitation in the Gulf of California. Contributions from the northeast possibly correspond to reflections off the San Bernardino mountains [Stich and Morelli, 2007]; excitation in the North Atlantic is less likely because of the missing seasonal variability [Stehly *et al.*, 2006].

[25] The observed ZZ summer and winter distributions are remarkably similar, suggesting seasonally stable near-coastal excitation. The associated ZR winter intensity from the southwest is larger than the ZZ winter intensity, i.e., $\text{SNR}_{\text{ZR}} > \text{SNR}_{\text{ZZ}}$.

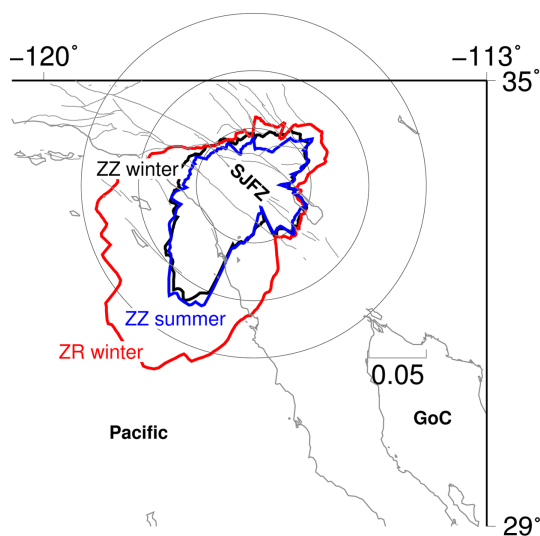


Figure 6. The distribution of noise intensity, $B(\theta)$, inferred from azimuthal SNR distributions (0.1–0.45 Hz), is a consequence of near-coastal microseism excitation. The center of the rose diagram is aligned with the network center. Note the high resemblance of ZZ winter and summer distributions. SJFZ: San Jacinto fault zone. GoC: Gulf of California.

Although the ellipticity or HZ ratio, here the ratio of ZR to ZZ coherency amplitude, depends on velocity structure, frequency, and season [Tanimoto and Alvizuri, 2006; Tanimoto *et al.*, 2006], it is invariant for negative and positive lags of Green’s functions approximations. Consider the station pair PLM–PMD oriented perpendicular to the coast (Figures 1b and 5b). Because the signal (coherency amplitude) ratio is similar for both directions, but SNR_{ZR} for PLM→PMD is larger, it requires excess incoherent noise in ZZ functions compared to remnant fluctuations in ZR away from the coast.

[26] Results of the correlation function-based analysis of wave field properties are compatible with the hypothesis suggested by the initial length-scale analysis: The distance between the 5 s microseism source region and the study area is too small to facilitate multiple scattering and thus isotropic propagation. Anisotropic noise properties derived from phase (beam-forming) and amplitude (B estimates) patterns indicate that the scattered wave field is not equipartitioned [Hennino *et al.*, 2001; Paul *et al.*, 2005]. However, in contrast to results of Larose *et al.* [2007] and Hillers *et al.* [2012a], evidence for the ballistic propagation regime can not be inferred. The interaction of microseism noise with the heterogeneous medium produces wave field properties that are characterized by scattered propagation [Gouédard *et al.*, 2008]. In summary, anisotropic flux is controlled by the proximity to the constantly acting source, yet medium heterogeneity, although not sufficient to completely randomize propagation directions, promotes scattered propagation.

4. Validity and Limits of Noise Imaging in the Study Area

[27] The joint length scale and wave field analysis related the medium properties to the observed characteristics of the ambient wave field. We now investigate the implications of the resulting incomplete reconstruction of Green’s functions, consequences of the nearby excitation coupled to incomplete randomization, on noise imaging in the SJFZ area. The dimension of the network is an order of magnitude larger than the array used by Roux *et al.* [2011] to image the low-velocity zone of the San Andreas fault near Parkfield. The SJFZ network is thus suited for regional imaging but high-resolution fault imaging may benefit from an increased network density around the fault. We

therefore focus on first-order estimates of velocity contrasts and attenuation patterns using phase and amplitude information from the C -function database.

4.1. Technical Aspects

[28] Surface wave arrivals are visually identified in the time-distance patterns (section 3.2). The associated timing and amplitude information are determined by searching for the peak envelope (Hilbert transform) in a time window of one period duration. To select good-quality phase and amplitude measurements, SNRs are converted to decibel before a linear trend is removed from the $\text{SNR}(r)$ population. Data associated with residual SNR larger than -2 times the standard deviation are considered in linear least-squares regressions.

4.2. Information from Phase

4.2.1. Velocity and Travel Time Error Estimates

[29] We estimate relative differences in the physical properties, indicated by systematic wave speed variations, of crustal materials bisected by the SJFZ. The above reported Rayleigh wave velocity $c = 2.79(\pm 0.02)$ km/s is an average least-squares fit obtained from ZZ winter C -functions in the 0.1–0.45 Hz band and all station bearings using interstation distances between 12 and 60 km. We do not find systematic deviations from this average considering subsets consisting of azimuths that are parallel or perpendicular to the dominant flux direction; this indicates relatively unbiased phase reconstructions associated with scattered propagation [Gouédard *et al.*, 2008].

[30] This observation is supported by estimates of the apparent error δt associated with nonisotropic $B(\theta)$ distributions [Weaver *et al.*, 2009; Froment *et al.*, 2010]

$$\delta t = \frac{B''(\theta_p)}{2t\omega_c^2 B(\theta_p)}, \quad (5)$$

where θ_p is the azimuth along the receiver pair direction and $\omega_c = 2\pi f_c$. For arrivals at $t = 5$ s the observed $B(\theta)$ distribution results in δt estimates for the ZZ winter stack in the interval $[-0.01, 0.02]$ s, with the majority between $[-0.005, 0.005]$ s. For arrivals at 20 s corresponding δt estimates cluster in the interval between ± 0.001 s. The theoretical bias introduced by the vicinity of the observation site to the source region is therefore small for the range of detector separations, consistent with the conclusion by Weaver *et al.* [2009].

However, future high-resolution noise-based tomography studies in the study area utilizing improved processing including more narrow frequency bands and station distances comparable to the wavelength, for which the effect gets amplified, can benefit from a δt correction.

4.2.2. Velocity Contrast

[31] The negligible δt bias allows us to study systematic velocity variations in the crust adjacent to the SJFZ. Following the spatial $\delta c/c$ distribution (Figure 2a), we separate the network into four subarrays: Stations southwest and northeast of the fault are split into arrays northwest and southeast of the Anza segment, respectively (Figure 1b). Because of the reduced number of stations in each subarrays, while maintaining the quality criteria for travel time readings, error estimates increase relative to the measurement on the full data set. The analysis is performed for narrow frequency bands centered between 0.15 and 0.9 Hz, analyzing C -functions obtained by bandpass filtering the 0.1–1.3 Hz signals. Interpreting the peak sensitivity of u_z eigenfunctions ($u_z > 0.8$; Figure 10) as a proxy for vertical resolution, the 0.15–0.9 Hz range translates into maximum depth sensitivity between 2 and 7 km (Figure 7).

[32] Southeast of Anza velocities to the southwest of the fault (subarray C) are significantly smaller

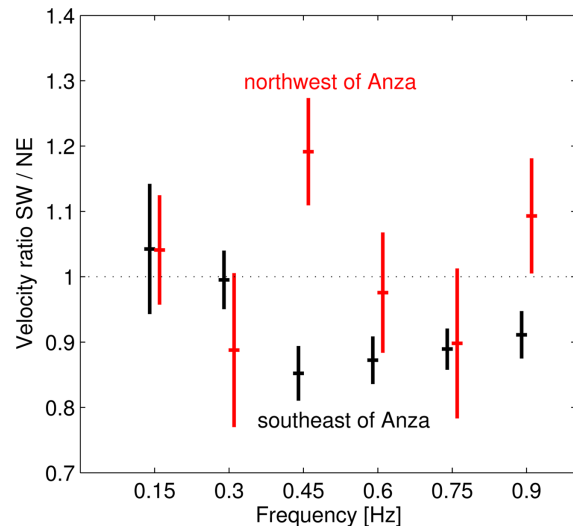


Figure 7. The dependence of velocity ratios measured in subarrays SW and NE to the fault on frequency indicates a depth-dependent velocity contrast across the arrays SE of Anza. Northwest and southeast of Anza correspond to subarrays (ratios) D/A and C/B, respectively. The sensitivity of the eigenfunctions $u_z > 0.8$ (0.5) corresponding to the six frequencies is limited to the top [7, 4, 3, 2, 2, 2] [11, 6, 4, 3, 3, 2] km.



compared to the northeast (B) for frequencies >0.4 Hz (black data in Figure 7), i.e., for depths shallower than ~ 3 km. A velocity contrast below ~ 4 km is not resolved. A region of higher wave speeds to the northeast of the trifurcation area (B) is also identified in the $\delta c/c$ maps for periods around 0.5 Hz (Figure 2a) [Allam and Ben-Zion, 2012]. The data from the two arrays northwest of Anza are more ambiguous (red data in Figure 7). Station connections in the northeast subarray (A) cover a transition area with fluctuating $\delta c/c$ signs (rejection of station KNW, shared with the subarray to the south, leaves too few data points for a regression). This coverage controls the mainly neutral velocity ratios. Only data at 0.45 Hz and 0.9 Hz indicate a relative decrease of the shallow velocity to the northeast (A). The northward offset of the high-velocity structure southwest (D) of the fault may be partially responsible for the alternating juxtaposition of relative high- and low-velocity features (Figure 2a).

4.3. Information from Amplitude: Attenuation Estimates

[33] The amplitude pattern provides information about attenuation properties. Ballistic surface wave amplitudes decay by geometric and material attenuation. The latter is composed of intrinsic and scattering attenuation, $Q^{-1} = Q_i^{-1} + Q_{sc}^{-1}$, and usually parameterized by $e^{-r\alpha(f)}$; the relation to the surface wave quality factor Q is $\alpha = \pi f / UQ$. Amplitudes can also be affected by detector gain, wave de-/focusing due to velocity variations, site amplification, source characteristics, internal scattering, and, relevant for noise correlation amplitudes, noise intensity and preprocessing choices. Internal scattering is expected to influence (high-frequency) data at near-fault stations due to the high-velocity gradient associated with the damaged material of the SJFZ [Allam and Ben-Zion, 2012]. Disentangling these many factors to estimate intrinsic and scattering attenuation of the medium is difficult. It requires independent information about wave field and medium properties to correlate spatial variations in α with actual variations in crustal properties. A key observation in this context constitute estimates of spatially average Q_{sc} (Table 1) that can potentially be used to narrow down Q_i in case of reliable Q measurements.

[34] Data processing and scaling of correlation functions is essential for consistent measurements of α [Larose et al., 2007; Prieto et al., 2009; Cupillard and Capdeville, 2010; Weaver, 2011;

Tsai, 2011]. Assuming a stationary, isotropic wave field Prieto et al. [2011] argue that attenuation of a coherent phase due to absorption, scattering and geometrical spreading can be estimated from properly scaled coherency amplitudes. Our processing results in coherency estimates that allow the analysis of distance-dependent amplitudes and therefore attenuation. However, as we have shown, properties of the ambient wave field are not compatible with isotropy, and hence we focus in our discussion on implications of anisotropic noise on attenuation estimates.

[35] We consider two amplitude (A) estimates. The peak envelope utilized in the picking process, and RMS value of the correlations in a window around the picked arrival [Weaver, 2011]. The slope of geometrically corrected $\log-A(r)$ observations, determined with a least-squares minimization, is the targeted attenuation coefficient α . Analysis of attenuation coefficient ratios across the four domains similar to Figure 7 (not shown) does not yield the expected inverse correlation with velocity patterns. Instead, we find that the results are governed by the azimuthal distribution of station connections. To illustrate this effect we choose two large subarrays that consist of stations on both sides of the fault (A+B and C+D, Figure 2), which allows us to study attenuation properties between stations connected by direct paths that are parallel and across the fault. This choice is inspired by the physical properties of tectonic features but somewhat arbitrary; as will be shown, it emphasizes the azimuthal dependency because of the approximately subparallel orientation of the SJFZ with the coast line. We make relative amplitude measurements in distance-windows of 11 km width centered on 10–60 km in 2 km intervals (Figure 8a). For 0.1–0.45 Hz data, the obtained attenuation ratio is consistently larger than unity, except for distances between 20 and 30 km. The observation is insensitive to the choice of amplitude determination (peak-envelope, RMS), season (winter, summer, all-season), frequency (0.1–0.45 Hz, 0.1–1.3 Hz), and component (ZZ, ZR).

[36] This attenuation pattern is not controlled by the sensitivity to tectonic features but by anisotropic noise propagation. Figures 8b and 8c show the azimuthal distribution of station pairs associated with measurements in Figure 8a. Controlled by the network geometry which is predominantly distributed in the along-strike direction (Figure 1), fault-parallel bearings are characterized by a northwest azimuth ($270^\circ < \theta < 360^\circ$; Figure 8b) whereas across-fault directions show a significant

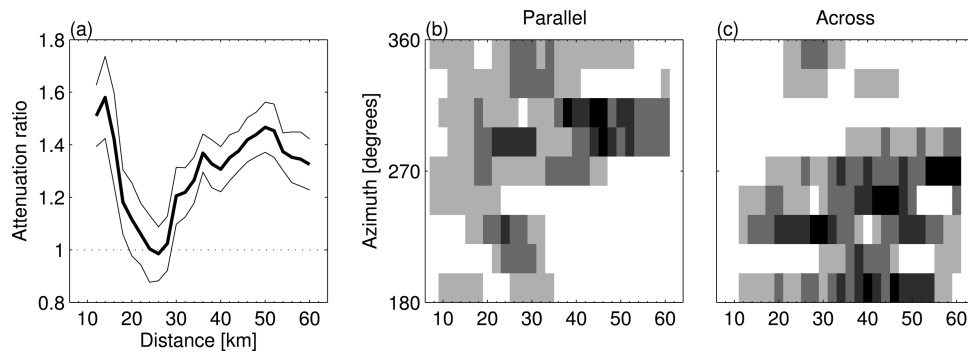


Figure 8. (a) The distance dependent ratio of the attenuation coefficient α is determined between estimates from station connections that do not cross the fault (mostly parallel to the fault) and estimates associated with across-fault bearings. (b, c) The associated azimuth distribution indicates a bimodal distribution (linear gray scale correlates with number of bearings in an azimuth/distance bin). Fault-parallel bearings are mostly oriented perpendicular to the main energy flux from the southwest quadrant ($180^\circ - 270^\circ$); fault-perpendicular bearings are parallel to the main propagation direction. Note that the distribution is not bimodal between 20 and 30 km.

southwest ($180^\circ < \theta < 270^\circ$; Figure 8c) orientation. Only where station connections that differ from the NE-SW direction are used in the α -fitting, the apparent signal vanishes; i.e., only between 20 and 30 km the azimuthal distribution of station connections is equilibrated. The location of the source region in the SW quadrant suggests geometric effects control the observed surface wave amplitude and hence apparent attenuation pattern: Relatively plane waves are traveling perpendicular to the fault strike, whereas scattered, predominantly radially spreading waves are propagating along the fault strike direction. Consequently, α associated with approximately 1-D planar wave attenuation perpendicular to the fault is lower compared to α associated with 2-D geometrical spreading, yielding the observed ratio-distance pattern [Gouédard *et al.*, 2008].

[37] We thus demonstrate that the amplitude pattern is controlled by the anisotropic noise intensity, consistent with previous conclusions on the sensitivity of C -amplitudes on distance and direction to the noise source [Weaver, 2011; Tsai, 2011]. For more robust attenuation estimates across the study area, several strategies can be conceived to mitigate problems associated with nonisotropic noise. For estimates of the 1-D Q structure following Prieto *et al.* [2009], the one sided far field surface wave extension of Tsai [2011] can be applied to the situation at hand. Neglecting the potential intensity decay with distance, a simultaneous inversion for attenuation, site factors, and intensity [Weaver, 2011] can use an independent assessment of $B(\theta)$ as discussed in section 3.3. A data-driven approach constitutes the analysis of amplitude pattern of C^3 -functions—correlations of the

coda of C -functions. Iterations of the correlation procedure yield better approximations of the Green's functions because of the increased isotropy of the C -coda wave field [Stehly *et al.*, 2008; Froment *et al.*, 2011; Hillers *et al.*, 2012a].

5. Discussion

[38] We examine the interaction of double-frequency microseisms with crustal heterogeneity in the southern California plate boundary area, using propagation and scattering length-scale analysis together with wave field properties inferred from noise correlation functions. Validity and limits of noise imaging in the context of the joint analysis are assessed by estimating physical properties of the SJFZ area from noise correlation functions.

[39] In the first part (section 2) we focus on the sensitivity of microseism propagation to medium heterogeneity. We find that double-frequency microseism scattering is sensitive to the high-frequency falloff of the fluctuation distribution best parameterized with a von Karman model [Holliger and Levander, 1992; Mai and Beroza, 2002; Sato and Korn, 2008]. The inferred scattering mean free path l [Frankel and Clayton, 1986] is comparable to the size of the network, yet smaller than the distance between the study area and the noise excitation region [Schulte-Pelkum *et al.*, 2004; Tanimoto *et al.*, 2006; Gerstoft and Tanimoto, 2007]. These relations ($d \geq l > a > \lambda$, equation (3)) control the noise propagation regime, which is expected to have a strong anisotropic component due to insufficient randomization of propagation directions. Yet average $Q_{sc} < 100$ estimates (Table 1) indicate a

relatively strong reduction of surface wave amplitude in the study area compared to shallow body wave attenuation [intrinsic and scattering in *Hauksson and Shearer, 2006*]. Results of the length-scale analysis provide an independent framework to interpret results from the subsequent noise correlation-based wave field analysis. This type of information is generally not available in the context of noise imaging and thus constitutes a key observation in the present study.

[40] In the second part (section 3), we analyze noise correlation functions to study the seasonal variability of prevalent noise constituents, excitation regions, and propagation patterns. Correlation functions are dominated by Rayleigh waves; the propagation pattern is seasonally invariant and suggests a constant near-coastal excitation off the southern California shoreline [*Schulte-Pelkum et al., 2004; Tanimoto et al., 2006*]. Our two times 100 day stacking is thus insensitive to variable contributions from excitation at more distant coastal stretches [*Gerstoft and Tanimoto, 2007*]. In contrast, slowness patterns of a near vertically incident teleseismic body wave arrival follows the seasonal variability of global microseism excitation. From an inversion of surface wave SNR we find anisotropic propagation directions, synonymous with an anisotropic intensity distribution. This observation can be interpreted in the context of the length-scale analysis. Wave field anisotropy reflects the governing effects of the nearby source relative to randomization through scattering. Constant excitation in proximity to the study area together with a relatively large scattering mean free path prevent the wave field evolution toward a diffuse regime [*Larose et al., 2007*]. However, medium fluctuations are sufficient to promote scattered propagation [*Gouédard et al., 2008*].

[41] The third part investigates the consequences of the nearby excitation coupled to insufficient randomization on imaging results. We find that Rayleigh wave arrival time errors associated with the anisotropic intensity pattern (equation (5)) [*Froment et al., 2010*] do not bias significantly our arrival time measurements. Insignificant travel time errors facilitate the resolution of a velocity contrast at depths shallower than 3–4 km in the region southeast of Anza (Figure 7); for areas to the northwest the measurements are more ambiguous and do not show a clear polarity. We conclude that the imperfect reconstruction of interstation Green's function estimates associated with anisotropy allows the resolution of a velocity contrast

across the SJFZ from noise correlations. However, arrival time errors become important at higher frequencies and at decreasingly separated stations [*Weaver et al., 2009*] and should be considered in high-resolution travel time inversions.

[42] Considering correlation amplitude information, we find that the proximity of the study area to the noise source region prohibits a standard inversion for attenuation properties. We show that attenuation estimates are biased by amplitude pattern that are associated with wave field instead of medium properties. Consistently reduced coast- and fault-perpendicular attenuation compared to coast- and fault-parallel estimates suggests that geometrical spreading factors control the amplitude pattern of DF Rayleigh waves. That is, waves emanated along the coast line are characterized by an increased planarity and hence subject to reduced attenuation relative to more radially spreading scattered waves associated with fault-parallel directions.

[43] The results of our analysis on propagation and scattering length scales and wave field properties challenge basic assumptions governing the reconstruction of interstation Green's function estimates from correlations of noise in the southern California plate boundary area. The DF microseism wave field is not characterized by equipartition or even isotropy [*Paul et al., 2005*]. The difficulty to reconstruct the amplitude is a general problem in noise imaging. Additional challenges for attenuation estimates in fault zone environments arise from internal scattering at fault structures characterized by a high-velocity gradient. Wave field properties thus change corresponding to the multi-length-scale character of fault zone architecture [*Ben-Zion and Sammis, 2003*]. Fault zone scattering properties motivates the development of alternative imaging methods that are sensitive to scale-dependent differences of scattered wave field properties.

[44] The velocity contrast southeast of Anza indicates a juxtaposition of different lithologies across the SJFZ. The velocity ratios are associated with horizontal averages over tens of kilometers on both sides of the fault (Figure 2a) and are in general agreement with broad-wavelength contrasts observed by previous imaging studies [e.g., *Scott et al., 1994; Tape et al., 2009; Allam and Ben-Zion, 2012*]. The degree of observed velocity contrasts differs among these including our study, which can “largely be explained by differences in data sets and resolution of the employed methods” [*Allam and Ben-Zion, 2012*]. Similar to other regional studies, the damage zone

observed by e.g., *Lewis et al.* [2005] and *Yang and Zhu* [2010] is not resolved in our 1-D approach. However, the station configuration is expected to facilitate the resolution of the low-velocity channel associated with damaged material in future noise-based surface wave traveltime tomographic inversions. Of particular interest for the assessment of material properties is the anticipated increase in isotropy of the near-fault wave field due to scattering associated with the damage zone material; increased C -function symmetry may be antagonized by reduced SNR levels due to the strong attenuation character of the Earth response. Augmented by sensors across the fault, fault zone trapped or head waves may be extracted from the ambient seismic field to invert for properties of trapping structures [*Hough et al.*, 1994; *Ben-Zion*, 1990; *Li et al.*, 1994; *Zhao et al.*, 2010].

[45] The feasible reconstruction of trapped or guided waves is anticipated to constitute a further noise-based technique to image complex fault zone environments. In general, surface wave noise-based imaging in active fault zone areas improves results from traditional earthquake tomography by the better resolution at shallow depths, thus mitigating resolution limits of predominantly vertically incident body waves. Improved knowledge about the velocity structure in the top few kilometers around active faults is essential for improved assessment of near-fault strong ground shaking. Moreover, noise-based tomography is not limited by the potentially heterogeneous distribution of data, thus improving the mapping of the variability of potential shaking in the fault vicinity. Disadvantages of noise-based techniques in the context of active fault zones include the limited frequency range and anisotropy of the noise sources. Also, many small earthquakes may escape data quality measures, leading to lower SNR levels; in case of strongly anisotropic (micro-) seismicity distributions, arrival times in correlation functions can be biased in analogy to anisotropic B distributions.

[46] In general, it is important to verify that surface wave arrival time estimates are not biased by asymmetric intensity or attenuation distributions, or incident body wave arrivals, which is particularly relevant for small sensor spacings compared to the wavelength. In addition to images obtained from variations of phase arrivals, efforts to extract reliable amplitude information, accounting for the effects discussed above, can provide important complementary information of material properties in fault zone environments.

Appendix A: Estimates of Scattering Properties from a 3-D Velocity Model

[47] We discuss the estimate of the scattering mean free path l from a regional 3-D high-resolution velocity model following the analysis of *Frankel and Clayton* [1986]. Statistical properties of the heterogeneous medium are parameterized by the autocorrelation of the spatial fluctuation distribution, and in the wave number domain by the fluctuation power spectrum $P(k)$. Because for a wave at wave number k the scattered energy at angle θ is proportional to $P(k)$ at radial wave number k_r , scattering attenuation $Q_{sc}^{-1}(k)$ can be expressed as the integral of $P(k)$ over the range of scattering angles θ [*Frankel and Clayton*, 1986, equation (C10)]

$$Q_{sc}^{-1}(k) = 2k^2\sigma^2 \int_{\theta_{\min}}^{\pi} P(k_r) d\theta. \quad (A1)$$

[48] Here $k_r = 2k\sin(\theta/2)$, $k = \omega/c$, ω and c are angular frequency and wave speed, and σ^2 denotes the fluctuation variance. Recall that “ Q_{sc}^{-1} equals the [fractional] energy loss $[\Delta E/E]$ per unit travel distance divided by k ” [*Frankel and Clayton*, 1986]. In the derivation of *Frankel and Clayton* [1986] the unit travel distance corresponds to the scatterer dimension; it is synonymous with the definition of the scattering mean free path, which is thus related to Q_{sc} [*Campillo*, 2006]

$$l = \frac{Q_{sc}(k)c}{\omega} = \frac{Q_{sc}(k)}{k}. \quad (A2)$$

$\Delta E/El$ is therefore proportional to the scattering attenuation coefficient α usually determined from amplitude measurements [*Wu*, 1982] (note the factor 2 difference between energy- Q and amplitude- Q [*Aki and Richards*, 1980]). We apply this approach to estimate l in a crustal volume ($270 \times 105 \times 29 \text{ km}^3$; Figure 1a) around the SJFZ from the velocity fluctuations of a high-resolution (1 km^3) $\alpha = v_p, \beta = v_s$ tomographic image [*Allam and Ben-Zion*, 2012].

[49] We clarify some persistent confusion in the literature associated with scaling and terminology of spectral estimates. We begin with the *unscaled* power spectrum, which may be better termed spectral power *density*, since it describes the spectral power of a stochastic process. Following *Buttkus* [1991], we call this spectral power density $G(k)$. This unscaled power spectral density and the (auto)covariance $R_{xx}(r)$ of a random 1-D distribution $x(r)$ form a Fourier pair (Wiener-Khinchine theorem), $R_{xx} \leftrightarrow F[G(k)]$, with $F[\]$ denoting the Fourier transform:

$$R_{xx}(r) = \int_{-\infty}^{+\infty} G(k)e^{i\omega r} dk. \quad (A3)$$



[50] At zero lag,

$$\sigma^2 = R_{xx}(0) = \int_{-\infty}^{+\infty} G(k)dk, \quad (\text{A4})$$

which is the analogy to Parseval's theorem [Buttkus, 1991]. In practice lower and upper integration limits are replaced by zero and the Nyquist wave number associated with a discretized distribution, respectively. The connection between R_{xx} and the correlation C_{xx} is simply

$$C_{xx}(r) = \frac{R_{xx}(r)}{R_{xx}(0)} = \frac{R_{xx}(r)}{\sigma^2}, \quad (\text{A5})$$

with σ^2 the variance from equation (A1). Consequently, the associated Fourier pair reads $C_{xx} \leftrightarrow F[G(k)/\sigma^2]$. For reliable estimates of $G(k)$ it is now important to apply the appropriate scaling during processing. Equation (A4) helps to verify the method. We discuss the procedure, applied to the 2-D case associated with horizontal $(\delta c/c)_\omega$ slices of the 3-D model below, using a stochastic 1-D distribution. The MATLAB code in Figure 9a demonstrates the determination of $G(k)$ for a random process, and verifies it by comparing it to alternative ways of computing σ^2 . Maintaining the consistency with the Wiener-Khinchine theorem underlying equation (A1), one has to consider equation (A5) and therefore use the *scaled* power spectral density $P(k) = G(k)/\sigma^2$ to evaluate the scattering potential. For the case of the (depth dependent) horizontal 2-D distributions of velocity variation in the SJFZ area the latter three estimates (var, mean, prod) of the scheme in Figure 9a are not available, since the distributions are not random. Hence we compute $P(k)$ from the 2-D Fourier transform of the spatial velocity perturbations using the scaling operations applied in the 1-D example. The computation of $G(k)$ is not reproduced here.

[51] Applying the methodology to estimate l for microseisms, we determine $P(k)$ functions associated with velocity perturbations $(\delta c/c)_\omega$ of Rayleigh waves. Neglecting density perturbations, Rayleigh phase speed variations for a given frequency ω are expressed as depth integrals over properly weighted (layer dependent) α and β variations [Aki and Richards, 1980, equation (7.88); see also Snieder, 1986]:

$$\left(\frac{\delta c}{c}\right)_\omega = \frac{1}{4k^2 U c I_1} \left[\int_0^\infty W_\alpha \left(\frac{\delta \alpha}{\alpha}\right) dz + \int_0^\infty W_\beta \left(\frac{\delta \beta}{\beta}\right) dz \right]. \quad (\text{A6})$$

```
(a)
dr = 2; %sampling interval
R = randn(1000,1);
mr = mean(R);
R = (R-mr)/mr; % dimensionless
nr = length(R);
nfft = 2^nextpow2(nr);
FFT = fft(R,nfft);
np = ceil((nfft+1)/2);
G = abs(FFT(1:np));
% 'dimensionalize' G; in 2D: dx*dy
G = G.^2/nr*dr;
G(2:end-1) = G(2:end-1)*2;
k = (0:np-1)/dr/nfft;
dk = k(2)-k(1);
% estimate the variance
sgm.int = trapz(G)*dk;
% alternative estimates
sgm.var = var(R);
sgm.mean = mean(R.^2);
sgm.prod = 1/(nr-1)*R'*R;
sgm =
    int: 1.3278e+03
    var: 1.3291e+03
    mean: 1.3278e+03
    prod: 1.3291e+03
```

```
(b)
% get G(k) [km^2] and k [1/km];
% get k of target f. ktarg;
% estimate the variance
sgmint = trapz(G)*dk*dk;
% resample G(k) > G(theta)
thmin = 30*pi/180;
thmax = pi;
dth = pi/100;
thrange = [thmin/2:dth:thmax/2];
ktheta = 2*ktarg*sin(thrange);
Gtheta = interp1(k,G,ktheta);
% estimate 1/Q using the
% scaled power spectral density
integral = trapz(Gtheta/sgmint)*dth;
Qinv = 2*ktarg^2*sgmint*integral;
% scattering mean free path
l = 1/(Qinv*ktarg);
```

Figure 9. MATLAB code examples associated with estimates of $G(k)$, Q_{sc} , and l . (a) Computation of the variance from a spectral estimate $G(k)$ of a random distribution. (b) Computation of l from $G(k)$. In the present application, the $G(k)$ function is obtained from the 2-D $\delta c/c$ distributions. $P(k)$ from equation (2ff.) equals $G\theta/sgmint$.

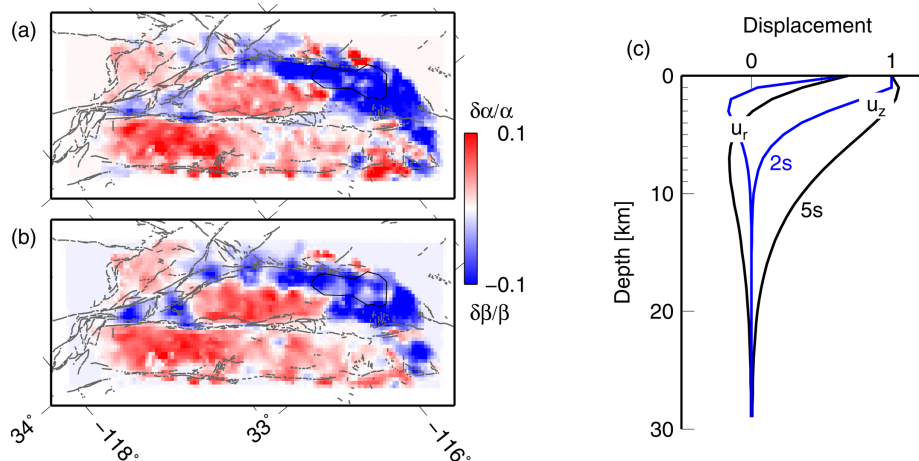


Figure 10. (a) P- and (b) S-wave velocity fluctuations $\delta\alpha/\alpha$, $\delta\beta/\beta$ in the study area at 3 km depth. (c) Rayleigh eigenfunctions $u_{[z,r]}$ for periods of 2 s and 5 s.

[52] The scaling factor depends on the wave number associated with ω , group and phase velocity U and c , and the energy integral I_1 . U is computed using equation (7.76) in *Aki and Richards* [1980], and depends on three energy integrals I_1 – I_3 . The I and W functions further depend on elastic constants ρ , λ , and μ , the vertical eigenfunctions of the fundamental-mode Rayleigh wave, u_z and u_r (Figure 10c) [Herrmann, 2006], and their derivatives $du_{[z,r]}/dz$. We use $\rho = 2.3 \text{ g/cm}^3$, and λ and μ are derived from α and β data [Allam and Ben-Zion, 2012]. Fluctuation properties of the $\delta c/c$ maps in the spectral domain, $G(k)$, are obtained considering the scaling operations displayed in Figure 9a. Choosing a proper lower integration limit (equation (A1)) we can deduce the Rayleigh wave scattering mean free path (Figure 9b).

Acknowledgments

[53] Data were retrieved from the Southern California Earthquake Data Center. GH thanks P. M. Mai and A. Obermann for discussions on random fields, and B. Froment for helpful feedback concerning intensity distributions. We thank the Associate Editor and two anonymous reviewers for comments that helped to improve the manuscript. This work was supported by the European Research Council (Advanced grant Whisper L27507). GH acknowledges support through a Heisenberg fellowship from the German Research Foundation. YBZ acknowledges support from the National Science Foundation (grant EAR-0908903). Some figures were made using GMT [Wessel and Smith, 1991].

References

Aki, K., and P. G. Richards (Eds.) (1980), *Quantitative Seismology*, 1st ed., 932 pp., W. H. Freeman, San Francisco, Calif.

Allam, A. A., and Y. Ben-Zion (2012), Seismic velocity structures in the Southern California plate-boundary environment

from double-difference tomography, *Geophys. J. Int.*, *190*, 1181–1196, doi:10.1111/j.1365-246X.2012.05544.x.

Ardhuin, F., E. Stutzmann, M. Schimmel, and A. Mangeny (2011), Ocean wave sources of seismic noise, *J. Geophys. Res.*, *116*, C09004, doi:10.1029/2011JC006952.

Ben-Zion, Y. (1990), The response of two half spaces to point dislocations at the material interface, *Geophys. J. Int.*, *101*, 507–528.

Ben-Zion, Y., and K. Aki (1990), Seismic radiation from an SH line source in a laterally heterogeneous planar fault zone, *Bull. Seismol. Soc. Am.*, *80*(4), 971–994.

Ben-Zion, Y., and C. G. Sammis (2003), Characterization of fault zones, *Pure Appl. Geophys.*, *160*, 677–715.

Bromirski, P. D., and F. K. Duennbier (2002), The near-coastal microseism spectrum: Spatial and temporal wave climate relationships, *J. Geophys. Res.*, *107*(B8), ESE 5-1–ESE 5-20, doi:10.1029/2001JB000265.

Bulut, F., Y. Ben-Zion, and M. Bonhoff (2012), Evidence for a bimaterial interface along the Mudurnu segment of the North Anatolian Fault Zone from polarization analysis of P waves, *Earth Planet. Sci. Lett.*, *327*–*328*, 17–22, doi:10.1016/j.epsl.2012.02.001.

Buttkus, B. (Ed.) (1991), *Spektralanalyse und Filtertheorie in der angewandten Geophysik*, 1st ed., 650 pp., Springer, Berlin.

Campillo, M. (2006), Phase and correlation of ‘random’ seismic fields and the reconstruction of the green function, *Pure Appl. Geophys.*, *163*, 475–502, doi:10.1007/s00024-005-0032-8.

Carcolé, E., and H. Sato (2010), Spatial distribution of scattering loss and intrinsic absorption of short-period s waves in the lithosphere of Japan on the basis of the Multiple Laplace Time Window Analysis of Hi-net data, *Geophys. J. Int.*, *180*, 268–290, doi:10.1111/j.1365-246X.2009.04394.x.

Cupillard, P., and Y. Capdeville (2010), On the amplitude of surface waves obtained by noise correlation and the capability to recover the attenuation: A numerical approach, *Geophys. J. Int.*, *181*, 1687–1700, doi:10.1111/j.1365-246X.2010.04568.x.

Eberhart-Phillips, D., and A. Michael (1993), Three-dimensional velocity structure, seismicity, and fault structure in the Parkfield region, central California, *J. Geophys. Res.*, *98*, 15,737–15,758.

Essen, H.-H., F. Krüger, T. Dahm, and I. Grevemeyer (2003), On the generation of secondary microseisms observed in

- northern and central Europe, *J. Geophys. Res.*, *108*(B10), 2506, doi:10.1029/2002JB002338.
- Fialko, Y., D. Sandwell, D. Agnew, M. Simons, P. Shearer, and B. Minster (2002), Deformation on nearby faults induced by the 1999 Hector mine earthquake, *Science*, *297*, 1858–1862, doi:10.1126/science.1074671.
- Frankel, A., and R. W. Clayton (1986), Finite difference simulations of seismic scattering: implications for the propagation of short-period waves in the crust and models of crustal heterogeneity, *J. Geophys. Res.*, *91*(B6), 6465–6489.
- Friedrich, A., F. Krüger, and K. Klinge (1998), Ocean-generated microseismic noise located with the gräfenberg array, *J. Seismol.*, *2*, 47–64.
- Froment, B., M. Campillo, P. Roux, P. Gouédard, A. Verdel, and R. L. Weaver (2010), Estimation of the effect of nonisotropically distributed energy on the apparent arrival time in correlations, *Geophysics*, *75*(5), 85–93, doi:10.1190/1.3483102.
- Froment, B., M. Campillo, and P. Roux (2011), Reconstructing the Green's function through iteration of correlations, *C. R. Geosci.*, *343*, 623–632, doi:10.1016/j.crte.2011.03.001.
- Gerstoft, P., and T. Tanimoto (2007), A year of microseisms in southern California, *Geophys. Res. Lett.*, *34*, L20304, doi:10.1029/2007GL031091.
- Gouédard, P., P. Roux, M. Campillo, and A. Verdel (2008), Convergence of the two-point correlation function toward the Green's function in the context of a seismic-prospecting data set, *Geophysics*, *73*(6), 47–53, doi:10.1190/1.2985822.
- Haubrich, R. A., and K. McCamy (1969), Microseisms: Coastal and pelagic sources, *Rev. Geophys.*, *7*(3), 539–571.
- Hauksson, E., and P. M. Shearer (2006), Attenuation models (QP and QS) in three dimensions of the southern California crust: Inferred fluid saturation at seismogenic depth, *J. Geophys. Res.*, *111*, B05302, doi:10.1029/2005JB003947.
- Hennino, R., N. Trégoùres, N. M. Shapiro, L. Margerin, M. Campillo, B. A. van Tiggelen, and R. L. Weaver (2001), Observation of equipartitioning of seismic waves, *Phys. Rev. Lett.*, *86*(15), 3447–3450, doi:10.1103/PhysRevLett.86.3447.
- Herrmann, R. B. (2006), *Computer programs in seismology, vers. 3.30; An overview of synthetic seismogram computation, Tech. Rep.*, Saint Louis Univ., <http://www.eas.slu.edu/eqc/eqcps.html>.
- Hillers, G., M. Campillo, Y.-Y. Lin, K.-F. Ma, and P. Roux (2012a), Anatomy of the high-frequency ambient seismic wave field at the TCDP borehole, *J. Geophys. Res.*, *117*, B06301, doi:10.1029/2011JB008999.
- Hillers, G., N. Graham, M. Campillo, S. Kedar, M. Landès, and N. Shapiro (2012b), Global oceanic microseism sources as seen by seismic arrays and predicted by wave action models, *Geochem. Geophys. Geosyst.*, *13*, Q01021, doi:10.1029/2011GC003875.
- Holliger, K., and A. R. Levander (1992), A stochastic view of lower crustal fabric based on evidence from the Ivrea zone, *Geophys. Res. Lett.*, *19*(11), 1153–1156.
- Hong, T.-K., and W. Menke (2006), Tomographic investigation of the wear along the San Jacinto fault, southern California, *Phys. Earth Planet. Inter.*, *155*, 236–248.
- Hough, S. E., Y. Ben-Zion, and P. Leary (1994), Fault zone waves observed at the southern Joshua Tree earthquake rupture zone, *Bull. Seismol. Soc. Am.*, *84*, 761–767.
- Kedar, S. (2011), Source distribution of ocean microseisms and implications for time-dependent noise tomography, *C. R. Geosci.*, *343*, 548–557, doi:10.1016/j.crte.2011.04.005.
- Kedar, S., M. Longuet-Higgins, F. Webb, N. Graham, R. Clayton, and C. Jones (2008), The origin of deep ocean microseisms in the North Atlantic Ocean, *Proc. R. Soc. A*, *464*, 777–793, doi:10.1098/rspa.2007.0277.
- Landès, M., F. Hubans, N. M. Shapiro, A. Paul, and M. Campillo (2010), Origin of deep ocean microseisms by using teleseismic body waves, *J. Geophys. Res.*, *115*, B05302, doi:10.1029/2009JB006918.
- Larose, E., P. Roux, and M. Campillo (2007), Reconstruction of Rayleigh-Lamb dispersion spectrum based on noise obtained from an air-jet forcing, *J. Acoust. Soc. Am.*, *122*(6), 3437–3444, doi:10.1121/1.2799913.
- Larose, E., P. Roux, M. Campillo, and A. Derode (2008), Fluctuations of correlations and Green's function reconstruction: Role of scattering, *J. Appl. Phys.*, *103*, 114,907, doi:10.1063/1.2939267.
- Lewis, M. A., and Y. Ben-Zion (2010), Diversity of fault zone damage and trapping structures in the Parkfield section of the San Andreas Fault from comprehensive analysis of near fault seismograms, *Geophys. J. Int.*, *183*, 1579–1595, doi:10.1111/j.1365-246X.2010.04816.x.
- Lewis, M. A., Z. Peng, Y. Ben-Zion, and F. L. Vernon (2005), Shallow seismic trapping structure in the San Jacinto fault zone near Anza, California, *Geophys. J. Int.*, *162*, 867–881, doi:10.1111/j.1365-246X.2005.02684.x.
- Li, Y.-G., K. Aki, D. Adams, A. Hasemi, and W. H. K. Lee (1994), Seismic guided waves trapped in the fault zone of the Landers, California, earthquake of 1992, *J. Geophys. Res.*, *99*(B6), 11,705–11,722.
- Longuet-Higgins, M. S. (1950), A theory of the origin of microseisms, *Phil. Trans. R. Soc. London, Ser. A*, *243*, 1–35.
- Longuet-Higgins, M. S. (1953), Can sea waves cause microseisms?, in Proceedings of Symposium on Microseisms, 4–6 Sept. 1952, pp. 74–86, Arden House, Harriman, N. Y.
- Mai, P. M., and G. Beroza (2002), A spatial random field model to characterize complexity in earthquake slip, *J. Geophys. Res.*, *107*(B11), 2308, doi:10.1029/2001JB000588.
- McGuire, J., and Y. Ben-Zion (2005), High-resolution imaging of the Bear Valley section of the San Andreas Fault at seismogenic depths with fault-zone head waves and relocated seismicity, *Geophys. J. Int.*, *163*, 152–164, doi:10.1111/j.1365-246X.2005.02703.x.
- Nishizawa, O., and Y. Fukushima (2008), Laboratory experiments of seismic wave propagation in random heterogeneous media, in *Advances in Geophysics, Vol. 50: Earth Heterogeneity and Scattering Effects on Seismic Waves*, edited by H. Sato and M. C. Fehler, pp. 219–246, Academic, Amsterdam.
- Ozakin, Y., Y. Ben-Zion, M. Aktar, H. Karabulut, and Z. Peng (2012), Velocity contrast across the 1944 rupture zone of the North Anatolian fault east of Ismetpasa from analysis of teleseismic arrivals, *Geophys. Res. Lett.*, *39*, L08307, doi:10.1029/2012GL051426.
- Paul, A., M. Campillo, L. Margerin, E. Larose, and A. Derode (2005), Empirical synthesis of time-asymmetrical Green function from the correlation of coda waves, *J. Geophys. Res.*, *110*, B08302, doi:10.1029/2004JB003521.
- Powell, C. A., and A. S. Meltzer (1984), Scattering of P-waves beneath SCARLET in southern California, *Geophys. Res. Lett.*, *11*(5), 481–484.
- Prieto, G. A., J. F. Lawrence, and G. C. Beroza (2009), Anelastic Earth structure from the coherency of the ambient seismic field, *J. Geophys. Res.*, *114*, B07303, doi:10.1029/2008JB006067.
- Prieto, G. A., M. Denolle, J. F. Lawrence, and G. C. Beroza (2011), On amplitude information carried by the ambient seismic field, *C. R. Geosci.*, *343*, 600–614, doi:10.1016/j.crte.2011.03.001.
- Revenaugh, J. (2000), The relation of crustal scattering to seismicity in southern California, *J. Geophys. Res.*, *105*(B11), 25,403–25,422.

- Roux, P. (2009), Passive seismic imaging with direct ambient noise: application to surface waves and the San Andreas Fault in Parkfield, CA, *Geophys. J. Int.*, *179*, 367–373, doi:10.1111/j.1365-246X.2009.04282.x.
- Roux, P., W. A. Kuperman, and the NPAL Group (2004), Extracting coherent wave fronts from acoustic ambient noise in the ocean, *J. Acoust. Soc. Am.*, *116*(4), 1995–2003, doi:10.1121/1.1797754.
- Roux, P., K. G. Sabra, P. Gerstoft, W. A. Kuperman, and M. C. Fehler (2005), P-waves from cross-correlation of seismic noise, *Geophys. Res. Lett.*, *32*, L19303, doi:10.1029/2005GL023803.
- Roux, P., M. Wathelet, and A. Roueff (2011), The San Andreas Fault revisited through seismic-noise and surface-wave tomography, *Geophys. Res. Lett.*, *38*, L13319, doi:10.1029/2011GL047811.
- Sabra, K. G., P. Gerstoft, P. Roux, W. A. Kuperman, and M. C. Fehler (2005a), Surface wave tomography from microseisms in Southern California, *Geophys. Res. Lett.*, *32*, L14311, doi:10.1029/2005GL023155.
- Sabra, K. G., P. Gerstoft, P. Roux, W. A. Kuperman, and M. C. Fehler (2005b), Extracting time-domain Green's function estimates from ambient seismic noise, *Geophys. Res. Lett.*, *32*, L03310, doi:10.1029/2004GL021862.
- Sato, H., and M. C. Fehler (Eds.) (2008), *Earth Heterogeneity and Scattering Effects on Seismic Waves*, 1st ed., 476 pp., Academic, Amsterdam.
- Sato, H., and M. Korn (2008), Synthesis of vector-wave envelopes in random elastic media on the basis of the Markov approximation, in *Advances in Geophysics, Vol. 50: Earth Heterogeneity and Scattering Effects on Seismic Waves*, edited by H. Sato and M. C. Fehler, pp. 43–93, Academic, Amsterdam.
- Sato, H., M. C. Fehler, and T. Maeda (Eds.) (2012), *Seismic Wave Propagation and Scattering in the Heterogeneous Earth*, 2nd ed., 494 pp., Springer, Berlin.
- Schulte-Pelkum, V., P. S. Earle, and F. L. Vernon (2004), Strong directivity of ocean-generated seismic noise, *Geochem. Geophys. Geosyst.*, *5*, Q03004, doi:10.1029/2003GC000520.
- Scott, J. S., T. G. Masters, and F. L. Vernon (1994), 3-D velocity structure of the San Jacinto fault near Anza, California—I. P waves, *Geophys. J. Int.*, *119*, 611–626.
- Seats, K. J., J. F. Lawrence, and G. A. Prieto (2012), Improved ambient noise correlation functions using Welch's method, *Geophys. J. Int.*, *188*, 513–523, doi:10.1111/j.1365-246X.2011.05263.x.
- Shapiro, N. M., and M. Campillo (2004), Emergence of broadband Rayleigh waves from correlations of the seismic ambient noise, *Geophys. Res. Lett.*, *31*, L07614, doi:10.1029/2004GL019491.
- Snieder, R. (1986), The influence of topography on the propagation and scattering of surface waves, *Phys. Earth Planet. Inter.*, *44*, 226–241.
- Stehly, L., M. Campillo, and N. M. Shapiro (2006), A study for the seismic noise from its long-range correlation properties, *J. Geophys. Res.*, *111*, B10306, doi:10.1029/2005JB004237.
- Stehly, L., M. Campillo, B. Froment, and R. L. Weaver (2008), Reconstructing Green's function by correlation of the coda of the correlation (c3) of ambient seismic noise, *J. Geophys. Res.*, *113*, B11306, doi:10.1029/2008JB005693.
- Stich, D., and A. Morelli (2007), Reflection of seismic surface waves at the northern apennines, *Earth Planet. Sci. Lett.*, *259*, 149–158, doi:10.1016/j.epsl.2007.04.036.
- Stutzmann, E., F. Ardhuin, M. Schimmel, A. Mangeney, and G. Patau (2012), Modelling long-term seismic noise in various environments, *Geophys. J. Int.*, *191*, 707–722, doi:10.1111/j.1365-246X.2012.05638.x.
- Tanimoto, T., and C. Alvizuri (2006), Inversion of the HZ ratio of microseisms for S-wave velocity in the crust, *Geophys. J. Int.*, *165*, 323–335, doi:10.1111/j.1365-246X.2006.02905.x.
- Tanimoto, T., S. Ishimaru, and C. Alvizuri (2006), Seasonality of particle motion of microseisms, *Geophys. J. Int.*, *166*, 253–266, doi:10.1111/j.1365-246X.2006.02931.x.
- Tape, C., Q. Liu, A. Maggi, and J. Tromp (2009), Adjoint Tomography of the Southern California Crust, *Science*, *325*, 988–992, doi:10.1126/science.1175298.
- Thurber, C., H. Zhang, F. Waldhauser, J. Hardebeck, A. Michael, and D. Eberhart-Phillips (2006), Three-dimensional compressional wavespeed model, earthquake relocations, and focal mechanisms for the Parkfield, California, Region, *Bull. Seismol. Soc. Am.*, *96*(4B), S38–S49.
- Tsai, V. C. (2011), Understanding the amplitudes of noise correlation measurements, *J. Geophys. Res.*, *116*, B09311, doi:10.1029/2011JB008483.
- van Wijk, K., T. D. Mikesell, V. Schulte-Pelkum, and J. Stachnik (2011), Estimating the Rayleigh-wave impulse response between seismic stations with the cross term of the green tensor, *Geophys. Res. Lett.*, *38*, L16301, doi:10.1029/2011GL047442.
- Weaver, R. L. (2011), On the amplitudes of correlations and the inference of attenuations, specific intensities and site factors from ambient noise, *C. R. Geosci.*, *343*, 615–622, doi:10.1016/j.crte.2011.07.001.
- Weaver, R. L., B. Froment, and M. Campillo (2009), On the correlation of non-isotropically distributed ballistic scalar diffuse waves, *J. Acoust. Soc. Am.*, *126*(4), 1817–1826, doi:10.1121/1.3203359.
- Wegler, U. (2003), Analysis of multiple scattering at Vesuvius volcano, Italy, using data of the TomoVes active seismic experiment, *J. Volcanol. Geotherm. Res.*, *128*, 45–63, doi:10.1016/S0377-0273(03)00246-4.
- Wessel, P., and W. H. F. Smith (1991), Free software helps map and display data, *Eos Trans. AGU*, *72*, 441.
- Wu, R.-S. (1982), Attenuation of short period seismic waves due to scattering, *Geophys. Res. Lett.*, *9*(1), 9–12.
- Yang, H., and L. Zhu (2010), Shallow low-velocity zone of the San Jacinto fault from local earthquake waveform modeling, *Geophys. J. Int.*, *183*, 421–432, doi:10.1111/j.1365-246X.2010.04744.x.
- Zhang, J., P. Gerstoft, and P. M. Shearer (2009), High-frequency P-wave seismic noise driven by ocean winds, *Geophys. Res. Lett.*, *36*, L09302, doi:10.1029/2009GL037761.
- Zhang, J., P. Gerstoft, and P. D. Bromirski (2010), Pelagic and coastal sources of P-wave microseisms: Generation under tropical cyclones, *Geophys. Res. Lett.*, *37*, L15301, doi:10.1029/2010GL044288.
- Zhao, P., Z. Peng, Z. Shi, M. A. Lewis, and Y. Ben-Zion (2010), Variations of the velocity contrast and rupture properties of M6 earthquakes along the Parkfield section of the San Andreas fault, *Geophys. J. Int.*, *178*, 765–780, doi:10.1111/j.1365-246X.2009.04436.x.
- Zheglova, P., J. R. McLaughlin, S. W. Roecker, J. R. Yoon, and D. Renzi (2012), Imaging quasi-vertical geological faults with earthquake data, *Geophys. J. Int.*, *189*, 1584–1596, doi:10.1111/j.1365-246X.2012.05424.x.